Spectroscopy and nuclear dynamics of starburst galaxies

Vermaas, L.

4

Nuclear stellar dynamics and *K*-band mass-to-light ratios of Ultraluminous Infrared Galaxies

L. Vermaas and P. P. van der Werf

Abstract

We present high resolution K-band integral field spectroscopy of a small sample of nearby ultraluminous infrared galaxies (ULIRGs), and use the CO bandhead data to derive the kinematics of the stellar components in these systems. Dynamical masses are derived, considering both the rotation and velocity dispersion of the stellar components. These masses are combined with the extinction-corrected K-band luminosities to derive K-band stellar mass to light ratios. We discuss the main uncertainties in our analysis which are dominated by the inclination angle of the rotating stellar system and the measurement of the effective radius. Our results show M/L_K values which are lower (and in several cases much lower) than those of evolved elliptical galaxies, and this reflects the lower age of the K-band stellar population. Given that M/L_K correlates with starburst age, we look at evolutionary trends with M/L_K, but find none. We conclude that M/L_K measures the age of the most recent starburst in the system, which cannot easily be related to the evolutionary stage of the system. Finally, we suggest a way to use M/L_K in the analysis of the starbursts ULIRGs, where it has the advantage that it does not depend on photoionization models, which are known to fail in ULIRGs due to the preponderance of (ultra)compact HII regions.

4.1 Introduction

Ultraluminous infrared galaxies (ULIRGs) are spectacular systems with infrared luminosities $L_{\rm IR} \geq 10^{12} L_{\odot}$. Nearly all are strongly interacting merger systems with a large amount of molecular gas, while most of the interstellar matter is concentrated in the inner regions of these objects, with extreme nuclear starbursts. The energy source is a combination of starburst and an active galactic nucleus (AGN), in varying proportion, as derived from spectroscopy and imaging at wavelengths from radio to X-rays. ULIRGs have a range in infrared spectral energy distributions, which is often expressed in the ratio of flux in the 25 μm and the 60 μm bands:"cool" ULIRGs have a typical ratio $f_{25}/f_{60} \leq 0.10$, whereas for "warm" ULIRGs $f_{25}/f_{60} > 0.2$. Warm ULIRGs have compact, bright nuclei compared to cool ULIRGs.

The AGN-starburst connection has become a central issue with the discovery of the relation between stellar velocity dispersion and mass of the central black hole in spheroidal stellar systems (Magorrian et al. 1998, Ferrarese & Merritt 2000, Gebhardt et al. 2000). Given that elliptical galaxies are mainly old, this relation has to be put in place at their formation history. Since ULIRGs form stars at prodigious rates, $10^2 - 10^3\,M_{\odot}{\rm yr}^{-1}$, and often host an AGN as well, they may be regarded as local analogs to forming spheroids. These points have been emphasised in extensive studies by Genzel et al. (2001) and Tacconi et al. (2002). While these studies indicate that local ULIRGs evolve into intermediate mass rather than giant ellipticals, they are still the best available local laboratories for studying the processes occurring in more luminous high-z objects such as the sub-mm galaxies, which may be the sites of the coeval explosive buildup of stellar mass and a supermassive black hole.

A conceptually simple mechanism for establishing a relation between stellar mass and black hole mass is based on feedback from the AGN terminating star formation. Sanders et al. (1988) argue that ULIRGs are dust-obscured precursors of QSOs. On this evolutionary path, the AGN disperses the dust and gas, shifting the bulk of energy toward shorter wavelengths, eventually becoming an optically bright QSO. In the context of the coeval buildup of stellar mass and black hole mass, the dispersal of dust and gas would also terminate star formation, and thus provides a possible mechanism for establishing a relation between black hole mass and stellar mass: once the black hole becomes so massive that its feedback on the environment disperses the gas, it shuts down star formation and the stellar mass is fixed. The dispersal of the gas also limits further growth of the black hole. The stellar mass is then given by the integral of star formation over time during the ULIRG phase, the black hole mass by the integral of accretion rate over time.

If ULIRGs indeed evolve into elliptical galaxies, they should also show the characteristic scaling relations of elliptical galaxies, in particular the so-called Fundamental Plane (FP), which relates the effective radius $R_{\rm eff}$, the average surface brightness within $R_{\rm eff}$, and the central velocity dispersion of an elliptical galaxy. On the other hand, the location of a galaxy with respect to the FP depends on its mass to light ratio (M/L), and an important evolving young stellar population will have a different M/L than a quiescent elliptical galaxy. In this paper we therefore focus on the M/L ratio of ULIRGs as derived from our near-infrared integral field spectroscopic, AO-assisted data from SINFONI of a sample ULIRGs/QSOs. The data allow us to constrain the gravitational potential of the nuclear region as derived

Table 4.1 – Observed sources

Name	z	$\log(L_{ir}/L_{\odot})$	f_{25}/f_{60}	kpc/″
IRAS 01388-4618[a]	0.090289	12.03	0.12	1.79
IRAS F05189-2524	0.042563	12.09	0.26	0.84
IRAS F09111-1007	0.054141	11.95	0.11	1.07
IRAS F17208-0014	0.042810	12.33	0.05	0.86
IRAS F20551-4250	0.042996	11.98	0.15	0.86
Arp 220[a]	0.018126		0.06	0.36

[a] No new data is presented for these sources, they are included for comparison.

from the modelling of the observed profile of the stellar CO absorption features in these objects. The dynamical properties of the nuclear gas disks, determined from the same data, is described in Chapter 5 of this thesis.

4.2 Observations and data reduction

Six objects were selected from the IRAS Revised Bright Galaxy Sample (Sanders et al. 2003), for gas kinematics as well as for stellar kinematics. These datasets provide measurements of gas kinematics and stellar kinematics in the same dataset, but in this chapter we focus on only the stellar kinematics, and describe the gas kinematics separately in Chapter 5. For qualification as an ULIRG, $L_{ir} \geq 10^{12}$. The redshift criterion was $z \leq 0.12$, in order to have enough spatial resolution and to be able to detect stellar CO-bandheads. The sample spans a range in infrared colours, in order to have a "sequence" from cool to warm ULIRGs (QSOs), albeit with very limited statistics. The infrared colour is determined by the ratio of flux in the 25μm band and the 60μm band (f_{25}/f_{60}; < 0.2 qualifies as 'cool' and > 0.2 qualifies as 'warm'). While we observed 6 targets (Table 4.1), the CO bandheads were detected in only 5 of these, including Arp 220, which has been discussed in Chapter 3.

The objects were observed with SINFONI, the Spectrograph for INtegral Field Observations in the Near Infrared (1.1 - 2.45 μm), which is installed on UT4 of the VLT (Eisenhauer et al. 2003, Bonnet et al. 2004), with the Laser Guide Star facility was used for Adaptive Optics. Since no nearby bright field stars were available, tip-tilt correction was done on the optical nucleus of the objects. The intermediate platescale was used, with a field of view of 3″x3″onto 64x64 spatial pixels. Each of these pixels is projected onto 2218 spectral elements in the K-band, with a central wavelength of 2.2μm. This results in spatial pixels with a resolution of 0.05″x0.10″, and a spectral resolution $\lambda/\Delta\lambda$ of 4000.

For the pointings, an ABA'-nodding mode was used, i.e. object-sky-object with equal integration times of 900 s, with the A' frame slightly shifted with respect to the A frame. The total (on-source) integration time was 6x900 s, or 75 minutes in most cases. The observations

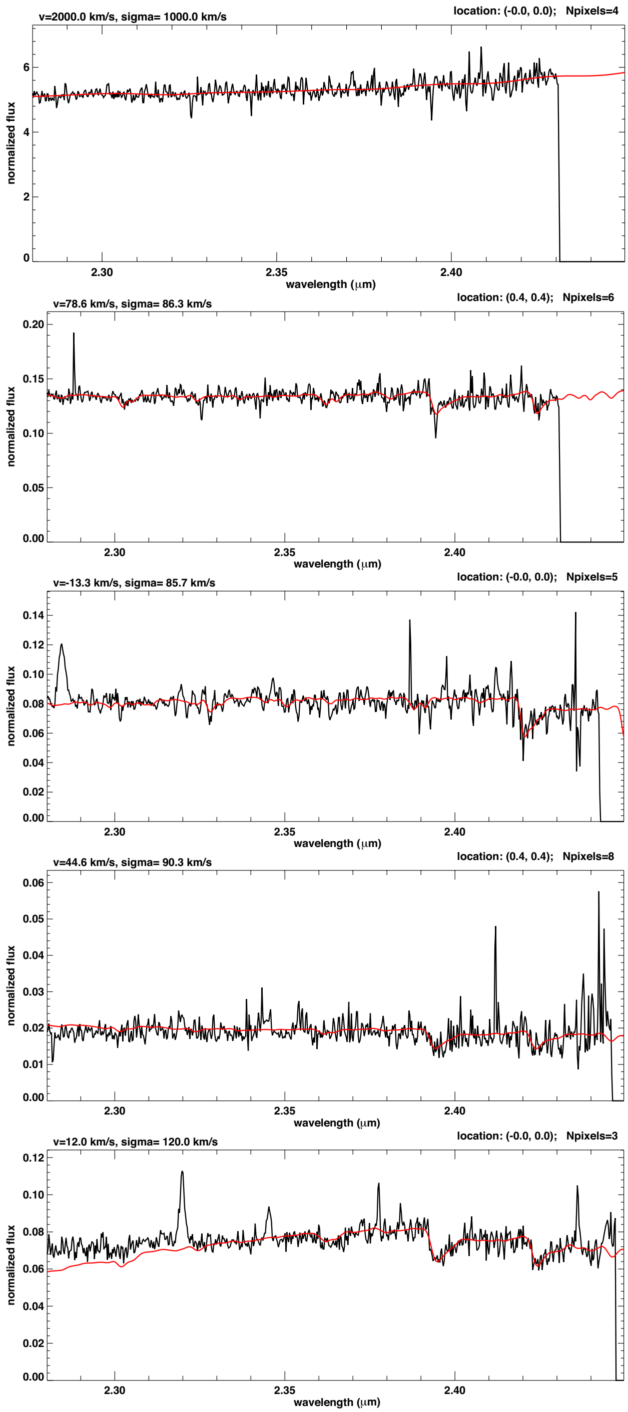

Figure 4.1 – Part of the K-band spectrum (black), with overplotted the PPXF-fit with 3-6 template spectra overplotted (red). Top to bottom: IRAS 05189-2524 nucleus, IRAS 05189-2524 outer location; IRAS 09111-1007 nucleus; IRAS 17208-0014 nucleus; IRAS 20551-4250 nucleus.

of IRAS 05189-2524 and IRAS 09111-1007 were carried out on December 29 and 30, 2007, with average seeing of 0.8″. The observations of IRAS 17208-0014 and IRAS 20551-4250 were carried out on July 18 and 19 of 2009 with an average seeing of 0.7″. Achieved Strehl ratios were of the order of 0.20-0.30.

The data were reduced with the SINFONI pipeline, which was developed by ESO and the Max-Planck-Institut für extraterrestrische Physik. The default procedure included corrections for pixel non-linearity, distortion and wavelength calibration.

For both flux calibration and telluric feature removal, a standard star was observed with the same setup as was used for the science frames, typically an early type star containing few stellar lines in the NAIR. After reduction, the average stellar spectrum was extracted and the stellar lines were removed (Br γ). Finally, each spectrum of the object frame was divided by this extracted spectrum.

In the case of IRAS 05189-2524 and IRAS 09111-1007, a PSF of 0.24″was determined from the [SiVI] line map of IRAS 09111-1007, which is assumed to originate from a point-source.For IRAS 17208-0014 and IRAS 20551-4250, the PSF-size was determined from observations of QSO Mrk 1014, in the same night, with the same instrumental setup and was measured to be 0.2″.

4.3 Results and analysis

In this paper, we focus on the stellar dynamics, while the gas morphology (H_2 2.12μm and Pa α) and kinematics are analysed and *K*-band spectra are presented in Chapter 5. In all of these objects, stellar absorption features of CO (^{12}CO 2-0 at 2.29μm and in some cases ^{12}CO 3-1 at 2.32μm) were detected (if not redshifted out of the *K*-band range).

4.3.1 Method

Deriving stellar kinematics

In order to derive stellar kinematics we followed the procedure described in Chapter 3. The parts of the *K* band nuclear spectra where the strongest CO-absorption features are present, were fitted with 6 stellar template spectra of different types, which originated from SINFONI observations as well. The Penalised Pixel Fitting (PPXF) from Cappellari & Emsellem (2004) was used for the fitting process. Before the fitting, the spatial pixels were combined according to the Voronoi method, and in our case a S/N of 20 for each bin was sufficient for high quality fits in order to obtain a coherent stellar velocity field. Fitted and measured spectra at the nuclear locations are shown in Fig. 4.1. Figure 4.2 shows for each galaxy the *K*-band continuum map, while Fig. 4.3 shows the resulting stellar velocity field (v_*) and the stellar velocity dispersion field (σ_*).

Dynamical mass estimate from σ_* and v_*

The dynamical mass $M_{\rm dyn}$ can be calculated from the stellar velocity dispersion, using

$$\frac{M_{\rm dyn}}{M_\odot} = 1.4 \cdot 10^6 \left(\frac{\sigma_*}{\rm km\,s^{-1}}\right)^2 \frac{R_{\rm eff}}{\rm kpc}, \quad (4.1)$$

where $R_{\rm eff}$ is the effective (half light) radius. This is an application of the general formula in Bender et al. (1992, Eq. 3), where the factor of $1.4 \cdot 10^6$ results from a constant M/L King model with $R_{\rm tidal}/R_{\rm core} = 50$: between a dwarf and a giant elliptical (Bender et al. 1992, Appendix A). For a spherical system with significant rotational support, this formula can be modified to the expression

$$\frac{M_{\rm dyn}}{M_\odot} = 4.7 \cdot 10^5 \left[3\left(\frac{\sigma_*}{\rm km\,s^{-1}}\right)^2 + \left(\frac{v_*}{\rm km\,s^{-1}}\right)^2\right] \frac{R_{\rm eff}}{\rm kpc}, \quad (4.2)$$

where v_* is the stellar velocity measured at $R_{\rm eff}$ (Appendix B of Bender et al. 1992, Dasyra et al. 2006, Davies et al. 2007).

The dynamical mass within a radius $R_{\rm out}$ is calculated assuming a Hernquist potential, which has the analytical property $M(r) = M_{\rm tot}\frac{r^2}{(r+a)^2}$, where a is related to the half-mass radius $r_{1/2}$ by $r_{1/2} = (1+\sqrt{2})\,a$ (Hernquist 1990). The mass within this radius, i.e. our field of view, can now be compared to the K-band luminosity in the same region.

Our calculation is quite sensitive to the value of $R_{\rm eff}$, the radius enclosing half the total light. Determinations of $R_{\rm eff}$ for ULIRGs are however strongly compromised by the large amounts of nuclear extinction. Since the extinction is typically highest at the nuclei, where the intrinsic surface brightness is highest, values of $R_{\rm eff}$ will be overestimated if nuclear extinction plays a role. In principle, an accurate extinction correction should be able to alleviate this problem, but accurate extinction corrections are challenging for these highly obscured systems. The fact that published values of $R_{\rm eff}$ (even from extinction corrected data) for the same ULIRG often depend on the observing wavelength illustrates the severity of this problem. Therefore, in stead of attempting to derive $R_{\rm eff}$ from an extinction corrected image, we circumvent the problem by noting that if M/L does not vary with radius, $R_{\rm eff}$ should equal the radius enclosing half of the total mass. We then use dynamically determined values of $R_{\rm eff}$, derived from the nuclear gas dynamics discussed in Chapter 5. The reader is referred to that chapter for further discussion.

The dynamical masses are also dependent on the presence of rotational dynamical support, and indeed rotation of the stellar component is observed in several of our targets. The importance of rotational support for the derived dynamical mass then depends on the assumed inclination of the rotational pattern. Our data are not sufficiently accurate that the inclination can be determined from the data themselves and we therefore assume the rotation of the stellar body to have the same inclination as the gas disks, as described in Chapter 5. Table 4.2 has a column v_*/σ_* which shows values both uncorrected and corrected for inclination. The resulting dynamical masses (including the inclination correction) are listed in the same table.

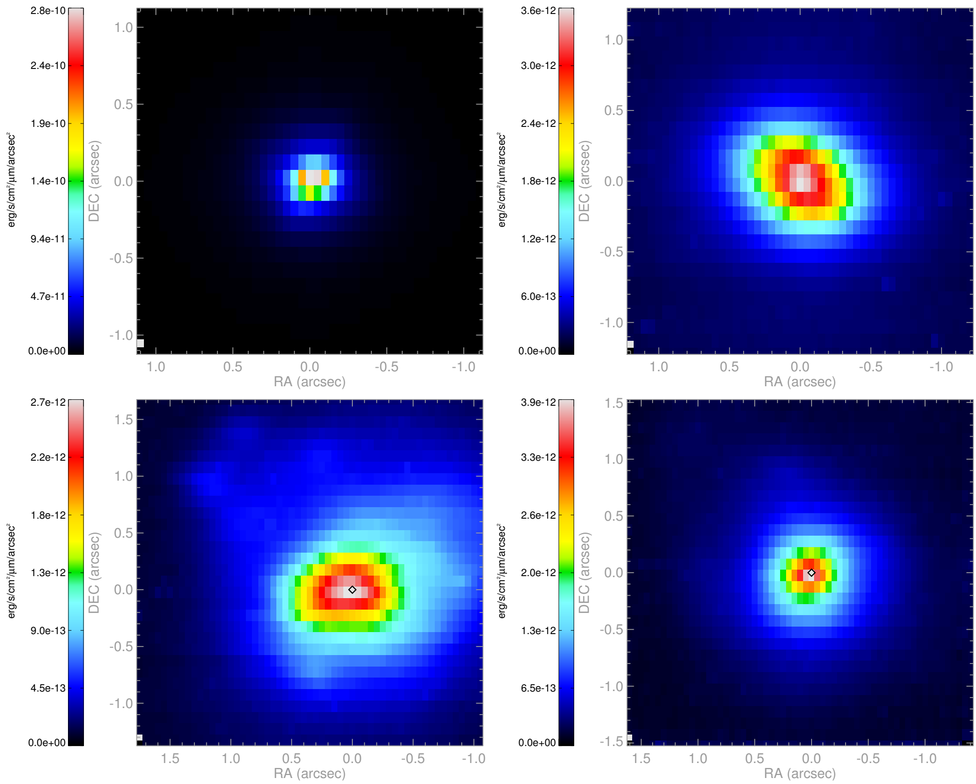

Figure 4.2 – *K*-band continuum; top left: IRAS 05189-2524; top right: IRAS 09111-1007; bottom left: IRAS 17208-0014; bottom right: IRAS 20551-4250.

K-band luminosity and extinction

In all cases except IRAS 05189-2524 (see below, Sect. 4.3.3), the *K*-band luminosity (L_K) was determined and extinction corrected from a pixel-to-pixel derived extinction map from the line ratio Pa α/Br γ, which has an intrinsic ratio of 12.07 (Hummer & Storey 1987). In regions where no reliable extinction measurement could be made, a value of A_K=0.7 was used, following Tacconi et al. (2002). The values of L_K (uncorrected and corrected for extinction) and $M_{\rm dyn}/L_K$, calculated for the extinction-corrected values of L_K are stated in Table 4.3.

4.3.2 IRAS 01388-4618

With f_{25}/f_{60} of 0.12, this is a "medium" ULIRG in the sample. This is the object where we could not measure the CO bands, due to the high redshift of 0.09. However, since we did measure its gas dynamics, we do include it in our sample and for the stellar kinematics we adopt ($v_* = 130 \pm 15$, $\sigma_* = 144 \pm 10$) km/s from Genzel et al. (2001). The *K*-band luminosity

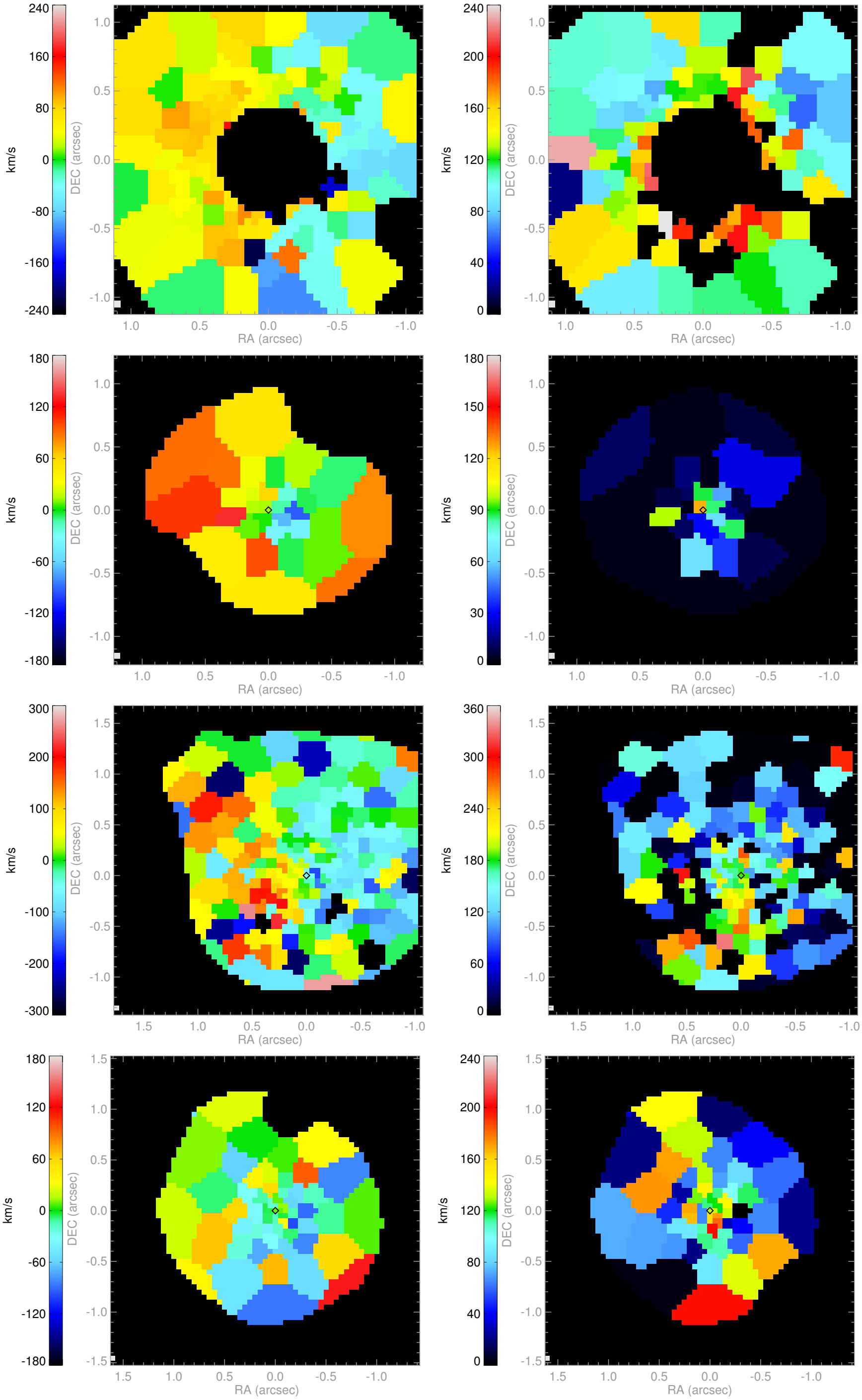

Figure 4.3 – Left: stellar velocity; right: stellar velocity dispersion. From top to bottom: IRAS 05189-2524, IRAS 09111-1007, IRAS 17208-0014 and IRAS 20551-4250. In all images, the (0,0) coordinate is located on the K-band continuum peak, which is also used as the kinematic centre, unless stated otherwise.

and extinction were determined from our SINFONI-data. The average nuclear value was $A_K \sim 1.1$, with a range of A_K between 0 and 1.8 over the whole region. Analysis of the gas dynamics (Chapter 5) using a combination of a spheroid and a disk resulted in an effective radius for the spheroid of 1.6 kpc, slightly outside the range 1.0 ± 0.4 kpc adopted by Genzel et al. (2001). With these values, the total dynamical mass from stellar kinematics is $(6.0 \pm 1.0) \cdot 10^{10} M_\odot$.

The inclination of the gas disk is 30°, and if this inclination is also assumed for the stellar spheroid, the corrected stellar rotation velocity of 260 km/s makes the mass increase by a factor of 1.6, resulting in an M/L_K of $0.06 \pm 0.02 M_\odot/L_{K,\odot}$. Chapter 5 also shows the presence of a disk component of containing 0.46 of the total dynamical mass within the region considered. However, since the (H-band) light profile of IRAS 01388−4618 accurately follows a De Vaucouleurs law (Genzel et al. 2001), the stellar light is dominated by the spheroid. It is possible that the disk is largely gaseous, which would result in a nuclear gas fraction of $\sim$ 50% which is a high value, but not outside the bounds of plausibility. Unfortunately, there is no direct measurement of the molecular gas mass available for this object. Note, however, that because of the relatively high redshift, the field of view covers the galaxy out to a radius of 2.4 kpc, which is significantly beyond $R_{\rm eff}$. The stellar/bulge component is more important in the central part and the gas fraction within the effective radius is lower (see the fit in Chapter 5). A correction for a ∼50% gas component would result in a M_*/L_K of $0.030 \pm 0.01 M_\odot/L_{K,\odot}$.

4.3.3 IRAS 05189-2524

This warm ULIRG has an approximately face-on orientation with literature values for the inclination of ∼20-30°. The K-band continuum map shows a compact and regular nucleus, with a strong peak. The stellar absorption bands could only be identified outside a radius of ∼0.4″(0.34 kpc) from the centre of the nucleus, which is most probably an effect of the AGN which contributes about 55% to the NIR continuum (e.g. Davies et al. 2007), diluting the absorption bands. The velocity field outside this region, however, shows regular stellar rotation with a maximum velocity of ∼85 km/s. The stellar velocity dispersion seems to rise towards the centre, reaching maximum detectable values of ∼180-200 km/s but the precise value is hard to determine.

The inclination used in the gas velocity model from Pa α (Chapter 5) is 22°. The fitted spheroid has an effective radius of 0.35 kpc, which is a factor 2 smaller than the photometric value found by Dasyra et al. (2006). Given the large contribution of the QSO to the nuclear light, which is not easily removed from the radial light profile, we here use our dynamically determined value for $R_{\rm eff}$. The kinematic major axis of the stellar velocity field is the same as for the gas, and they therefore likely have the same inclination. The inclination-corrected stellar rotation velocity is then 225 km/s, and the total dynamical mass is $1.8 \cdot 10^{10} M_\odot$. Within the radius $R_{\rm out}$=0.34 kpc (the radius out to which the gas kinematics was analysed), $M_{\rm dyn}$=$8.7 \cdot 10^9 M_\odot$.

Linemaps of Pa α and/or Br γ were not clean enough to determine a pixel-by-pixel extinction correction, and an average value of $A_K = 0.2$ was adopted from Severgnini et al. (2001), who derive this value for the inner 1.1″, using the near-IR line ratio Pa α/Pa β. The extinction corrected value of L_K is $3.89 \cdot 10^{11} L_{K,\odot}$. However, the AGN in IRAS 05189-2524 is estimated to be responsible for about 55% of the near-IR radiation (Davies et al. 2007; see also Nardini et al. 2009, Farrah et al. 2003). Then, only taking into account the stellar contribution to the luminosity, the K-band mass-to-light ratio $M_{\rm dyn}/L_{*,K}$ (=$M_*/L_{*,K}$) is $0.05 \pm 0.02\, M_\odot/L_{K,\odot}$, where we have used the inclination-corrected stellar rotation velocity.

4.3.4 IRAS 09111-1007

The K-band continuum shows an elongated distribution, with a position angle that is aligned with that of the stellar velocity field. The inclination derived from the axis ratio b/a fitted in the K-band is ∼40°. Stellar rotation is detected, but not defined very accurately and we estimate the value of v_* (uncorrected for inclination) to be ∼60-100 km/s. The stellar velocity dispersion shows values varying between 30 and 100 km/s around a single, unresolved peak of 130 km/s that coincides very accurately with the K-band centre, as well as with the peak of the [SiVI] line map detected in the K-band spectrum. This ULIRG thus harbours an AGN, but its contribution to the (near-)IR luminosity is probably very small (e.g. Farrah et al. 2003). A value of σ_* of 110 km/s was derived from a central aperture with a radius of ∼0.4″. The effective radius from the gas dynamical model (Chapter 5) is 2.3 kpc. The total dynamical spheroid mass from stellar kinematics (using an inclination-corrected rotation velocity) is $8.3 \pm 3.4 \cdot 10^{10} M_\odot$, the mass within a radius of 1.05 kpc (the radius out to which the gas kinematics was analysed) is $1.8 \pm 0.7 \cdot 10^{10} M_\odot$.

The pixel-by-pixel extinction map determined from the Pa α/Br γ line ratio shows K-band extinctions (A_K) between 0 and 1.6, with an average/maximum central value of $A_K = 1.5$. The value of $M_{\rm dyn}/L_K$ is $0.03 \pm 0.01\, M_\odot/L_{K,\odot}$ (using the extinction-corrected rotation velocity). The gas kinematic data indicates a disk component with a mass of 30% of the total mass for this object, or $M = 3.6 \cdot 10^9 M_\odot$. This is in excellent agreement with the gas mass $M = 3.1 \cdot 10^9 M_\odot$ derived for this object by Chung et al. (2009) using CO $1-0$ data. Correcting for this gas mass, the stellar mass to light ratio becomes $M_*/L_K = 0.02 \pm 0.01\, M_\odot/L_{K,\odot}$.

4.3.5 IRAS 17208-0014

This is the "coolest" ULIRG of the sample, with f_{25}/f_{60} of 0.05, while it is also the most luminous in the infrared. The K-band image shows a single nucleus, though the central part has no regular shape and the weaker parts also show some distortion features. The CO-absorption bands were detected with quite high S/N and the stellar rotation map could be derived with high resolution, showing regular rotation over the whole nuclear region. The stellar velocity dispersion map shows mean values of 40-150 km/s in the outer parts, rising to ∼250 km/s on a location that is offset south of the K-band nucleus position by 0.3″, a characteristic that is also detected in the gas velocity dispersion (Pa α, H_2), while the gas velocity field centres on the same location. However, also two bins with higher values (∼250 and 300 km/s) are detected 2″north of (0,0) and values are slightly higher (∼180 km/s) in between these two locations. In the gas kinematic (bulge+disk) model, the exponential disk

Table 4.2 – Stellar kinematics and dynamical mass.

Name	$R_{\rm eff}$	v_*	σ_*	i	v_*/σ_*	$M_{\rm dyn}$	$M_{\rm dyn}$(corr)
	(kpc)	(km/s)	(km/s)	(°)	uncorr/corr	$(10^{10} M_\odot)$	$(10^{10} M_\odot)$
(1)	(2)	(3)	(4)	(5)	(6)	(7)	(8)
IRAS 01388-4618[a]	1.6	$130^{\pm15}$	$144^{\pm10}$	30	0.9 / 1.8	$6.0^{\pm1.0}$	$9.8^{\pm1.8}$
IRAS F05189-2524[b]	0.35	$85^{\pm15}$	$137^{\pm16}$	22	0.6 / 1.6	$1.1^{\pm0.3}$	$1.8^{\pm0.5}$
IRAS F09111-1007	2.3	100^{100}_{68}	$110^{\pm20}$	38	0.9 / 1.4	$5.0^{\pm2.0}$	$8.3^{\pm3.4}$
IRAS F17208-0014	0.54	120^{150}_{100}	225^{275}_{160}	28	0.5 / 0.9	$4.2^{\pm2.0}$	$4.8^{\pm2.3}$
IRAS F20551-4250	1.5	$30^{\pm10}$	160^{200}_{80}	36	0.2 / 0.3	$5.5^{\pm3.5}$	$5.6^{\pm3.5}$
Arp 220[c]	2x0.2	$130^{\pm30}$	120^{150}_{100}	40	(1.1 / 1.4)	-	$1.2^{\pm0.4}$

Columns: (2) $R_{\rm eff}$ is derived from a Hernquist profile fit on the gas rotation curve from Paα or H_2 (see Chapter 5). (3) stellar rotation velocity (4) central stellar velocity dispersion (5) inclination, determined by gas disk dynamics or from K-band image. (6) (v_*/σ_*): left value is uncorrected, right value is corrected for inclination. (7) $M_{\rm dyn}$ is the total dynamical mass, calculated using both σ_* and v_*, with formula 4.2. The velocity is *not* corrected for inclination. The error is conservatively estimated by calculating the smallest and largest possible values using the limiting values of v_* and σ_*. (8) $M_{\rm dyn}$(corr) is the total dynamical mass with the stellar velocity corrected for inclination.

[a] Stellar CO absorption bands were redshifted out of the K-band; values of v_* and σ_* were adopted from Genzel et al. (2001).

[b] The CO absorption bands were not detectable in the central 0.4″(0.34 kpc) of the nucleus; v_* was measured outside the central region, the measured average value of σ_* on the inner edge is 120 km/s. The value stated is the value adopted from Dasyra et al. (2006).

[c] The analysis of this source is described in Chapter 3. $M_{\rm dyn}$ is calculated by summing the values calculated for each nucleus separately, while v_* of the fastest rotating nucleus has individually been corrected for an inclination of 50°. The value of v_*/σ_* is stated in brackets because the stellar nuclei have not merged yet, and only the value of the fastest rotating nucleus has been used.

Table 4.3 – Dynamical mass, K-band luminosity and M/L_K within R_{out}.

Name	R_{out}	M_{dyn}	L_K(uncorr)	L_K(corr)	M_{dyn}/L_K	M_*/L_K	Age (SB99)	
	(kpc)	$(10^{10}M_\odot)$	$(10^{10}L_{K,\odot})$	$(10^{10}L_{K,\odot})$	$\left(\frac{M_\odot}{L_{K,\odot}}\right)$	$\left(\frac{M_\odot}{L_{K,\odot}}\right)$	inst	cont
(1)	(2)	(3)	(4)	(5)	(6)	(7)	(8)	(9)
IRAS 01388-4618	2.4	$6.0^{\pm1.0}$	24.3	108	$0.06^{\pm0.015}$	$0.03^{\pm0.01}$	$13.5\,\mathrm{Myr}\,^{15}_{12}$	$<30\,\mathrm{Myr}$
IRAS F05189-2524	0.34	$0.87^{\pm0.25}$	32.1	17.5[a]	$0.05^{\pm0.017}$	$0.05^{\pm0.02}$	$15\,\mathrm{Myr}\,^{18}_{13}$	$\sim 50\,\mathrm{Myr}$
IRAS F09111-1007	1.05	$1.8^{\pm0.7}$	4.97	63.6	$0.03^{\pm0.013}$	$0.02^{\pm0.01}$	$11\,\mathrm{Myr}\,^{13}_{9}$	$<30\,\mathrm{Myr}$
IRAS F17208-0014	1.0	$3.3^{\pm1.6}$	4.73	10.7	$0.31^{\pm0.16}$	$0.27^{\pm0.16}$	$120\,\mathrm{Myr}\,^{240}_{32}$	$\sim 1.5\,\mathrm{Gyr}$
IRAS F20551-4250	0.9	$1.9^{\pm1.4}$	3.15	5.62	$0.34^{\pm0.26}$	$0.27^{\pm0.21}$	$120\,\mathrm{Myr}\,^{240}_{15}$	$\sim 1.5\,\mathrm{Gyr}$
Arp 220	0.6	$1.2^{\pm0.4}$	1.8	9.01	$0.13^{\pm0.04}$	$0.05^{\pm0.02}$	$15\,\mathrm{Myr}\,^{18}_{13}$	$\sim 50\,\mathrm{Myr}$

Columns: (2) R_{out} is the major axis length of an ellipse shape within the SINFONI field of view, for which gas dynamics is analysed in Chapter 5. M_{dyn}, L_K and M/L_K in this table are calculated within R_{out}. (3) Inclination corrected dynamical mass within R_{out}. (4) L_K(uncorr) is the total uncorrected K-band luminosity from the same dataset, measured within the ellipse with major axis R_{out}, expressed in solar K-band luminosities ($M_{K,\odot}$=3.28). The typical error in L_K is 10%. (5) L_K(corr) is corrected for extinction. The error in L_K(corr) is ~20%, based on the error in L_K(uncorr) and the extinction correction. (6) M_{dyn}/L_K within R_{out}, using extinction corrected value of L_K. (7) M_* is M_{dyn} with a gas component subtracted as described in the text. (8) Starburst age from M_*/L_K value for an instantaneous burst model, see text (Discussion). (9) Age from M_*/L_K value for continuous star formation with a star formation rate of $100\,M_\odot$/yr.

[a] For IRAS 05189-2524, an extinction correction of $A_K \sim 0.2$ was adopted from Davies et al. (2007), and a component of 55% has been subtracted for the AGN. The error estimate in L_K(corr) of IRAS 05189-2524 is 30%.

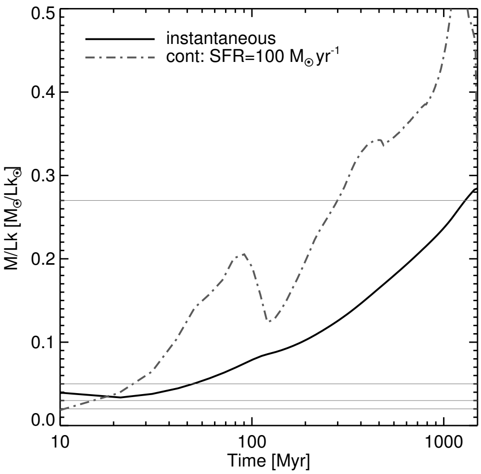

Figure 4.4 – Evolution of the K-band mass to light ratio from Starburst99, for a instantaneous burst (solid black line) and continuous star formation at a rate of $100\,M_\odot$ yr^{-1} (dot-dashed line). The horizontal grey lines denote M/L_K values derived for the targets in this work.

component was constrained to have the mass indicated by molecular gas (CO) data from Downes & Solomon (1998). The spheroid component was then fitted with an effective radius $R_{\rm eff}$ of 0.54 kpc. The gas fraction within the central region (out to $R_{\rm out}$=1.05 kpc) is 10%. An inclination of the gas disk of 27°was used for gas kinematic model, whereas from the K-band axial ratio it is estimated 35°. Using the conservative value of 35°, v_* becomes 209 km/s, resulting in a total $M_{\rm dyn}$=$4.8 \pm 2.3 \cdot 10^{10} M_\odot$ ($3.3 \pm 1.6 \cdot 10^{10} M_\odot$ out to $R_{\rm out}$=1.05 kpc).

The central extinction map from Brγ/Paα has values of A_K ranging from 0 to 2.0, with an average of $\sim$1.2. The extinction corrected value of $M_{\rm dyn}/L_K$ then is $0.31 \pm 0.16 M_\odot/L_{K,\odot}$ (using the stellar velocity corrected for inclination). Subtracting the 10% gas mass corrects this value to $M_*/L_K = 0.27 \pm 0.16 M_\odot/L_{K,\odot}$.

4.3.6 IRAS 20551-4250

Considering its infrared colours (f_{25}/f_{60}=0.15), this is a moderately warm ULIRG. The K-band nucleus is rather compact, but not as sharp as IRAS 05189-2524. The stellar velocity field does have signs of rotation, but the direction is not as clear as in the other objects. The value for rotation is estimated to be only 30 km/s. The velocity dispersion map has a peak of 200 km/s just south of (0,0), but consistent with the peak position in the K-band continuum image. The average velocity dispersion value was taken 120 km/s. The effective radius from bulge component of the gas kinematic fit was $R_{\rm eff}$=1.5 kpc, within the range estimated by Genzel et al. (2001). The axis ratio of the gas disk (Chapter 5) gives an inclination of 36°, different from that derived from the axis ratio of the K-band image, 17-25°. The effect on the dynamical mass is small (2% for 30° inclination, 12% for 20° inclination), and since the velocity field is not very regular, this effect is not taken into account.

The extinction map derived from Pa α/Br γ has values of A_K between 0 and 1.0, the average value is $A_K = 0.9$. The K-band mass-to-light ratio $M_{\rm dyn}/L_K$ is $0.34 \pm 0.26\,M_\odot/L_{K,\odot}$. Subtracting a gas fraction of 20% (the disk component of the gas dynamical fit) results in a M_*/L_K of $0.27 \pm 0.21\,M_\odot/L_{K,\odot}$.

4.4 Discussion

4.4.1 Uncertainties in mass determinations

Formula 4.1, calculating the dynamical mass from stellar velocity dispersion or also taking into account stellar rotation (Form. 4.2) are often used for mass determinations of spheroidal objects, e.g. by Tacconi et al. (2002), Dasyra et al. (2006), Davies et al. (2007). The reliability of the spectrum fit with one or more stellar templates, resulting in a velocity and a velocity dispersion is only one of the complicating factors. Rotation of the stellar component is taken into account, but deriving the inclination is not trivial and can be a major source of uncertainty. For face-on objects like IRAS 05189-2524, the effect can be quite large. Also, the resulting mass scales linearly with the assumed effective radius ($R_{\rm eff}$), defined as the radius within which half of the light is contained. Although the formula suggests one fixed value, $R_{\rm eff}$ is known to depend on the wavelength of the observation (Temi et al. 2008). We have avoided this uncertainty by using the effective radius as determined from the Hernquist-bulge potential (Hernquist 1990), which was used to fit a stellar spheroid (bulge) component to the gas rotation curve, thus resulting in a mass-based value rather than a light-based value. The value of the mass-based effective radius is generally smaller than the value determined from the light profile, which could be caused by high extinction in the nuclear region. The effect is described in more detail in Chapter 5. A further complication is the mass model. While we adopt a spherically symmetric Hernquist model, our K-band images show that for several objects spherical symmetry is at best only approximately correct. Furthermore, in at least one object a dynamically important disk component is found. In summary, even with our high quality data the derivation of dynamical masses is fraught with considerable uncertainties, and this is reflected by the error margins.

4.4.2 Uncertainties in luminosity determinations

The greatest uncertainty in the derived K-band luminosity is the extinction. Although we attempt to make extinction-corrections from near-IR line ratios, one should be aware of the fact that if extinctions are very high in (the very centre of) a nuclear region, radiation in the K-band emission is absorbed. For all of our sample ULIRGs, we find central values of A_K of ~ 1, which is what is to be expected when essentially looking at the edge of an optically thick region instead of into it. If this is the case, intrinsic values can be even higher.

4.4.3 M/L_K: expectations and implications

A summary of our M/L_K values is given in Table 4.3. While the uncertainties are considerable (see above), it is clear that the results separate into two groups: values of a few tenths and values of a few hundredths. All of our mass-to-light ratios are much lower than those of old ($> 10^{10}$yr), early type galaxies, consistent with the result of Tacconi et al. (2002), who also find the higher and comparable values for IRAS 17208-0014 and IRAS 20551-4250 (although not all of our objects are covered in their sample). The young implied ages also indicate at a significant (possibly dominant) fraction of the K-band light is contributed by the starburst, consistent with the conclusion by Engel et al. (2011) for Arp 220.

If an instantaneous burst of star formation would be responsible for the complete build-up of the stellar population, the ages corresponding to the mass-to-light ratios are typically (1-2)$\cdot 10^7$ yr for values of M/L_K between 0.02 and 0.05 (IRAS 01388-4618, IRAS 09111-1007, IRAS 05189-2524 and Arp 220), and (1-2)$\cdot 10^8$ yr for values of M/L_K between 0.2-0.4 (IRAS 17208-0014 and IRAS 20551-2450), column (9) of table 4.3. These ages are based on synthetic stellar population models of Starburst99 (Leitherer et al. 1999, Vázquez & Leitherer 2005), with a power law stellar initial mass function with slope α=2.35, solar metallicity ($Z_\odot$=0.020) and upper and lower mass cutoffs of 100 and 0.1 $M_\odot$, respectively, see Fig. 4.4. Note that using stellar population models with a lower mass cutoff of 1 $M_\odot$ (as sometimes proposed for starburst regions) increases the ages by a factor of at least 2 with respect to a lower mass cutoff of 0.1 $M_\odot$ which we adopt here. When assuming a constant star formation rate, the only period where values $M/L_K \leq 0.03$ are found, is in the first 10 Myr (see also Fig. 4.4). The value starts to gradually increase at $\sim$30 Myr (see column (10) of table 4.3). A value of 0.05 is reached at an age of $\sim$50 Myr, steadily rising to $M/L_K \sim 0.1$ at 1 Gyr, and further. This means that the ages for values of $M/L_K \leq 0.05$ are of the same order for an instantaneous burst and continuous star formation, but that values of $M/L_K \geq 0.2$ imply higher ages with continuous star formation ($>$ 1 Gyr) than for a burst. Since the high star formation rates for ULIRGs cannot be sustained over periods of the order of a Gyr, we consider only the ages implied by the instantaneous burst model.

4.4.4 An evolutionary path with M/L_K?

Given that the M/L_K appears to be rough age indicator, it is interesting to look for evolutionary trends with M/L_K. We do not find an evolutionary trend with infrared colour (f_{25}/f_{60}), which would confirm the scenario where these objects are on an evolutionary path from cool to warm ULIRGs to QSOs. While this may partly be due to small number statistics, it is remarkable that our coolest ULIRG (IRAS 17208−0014) has a high derived age, while our warmest ULIRG (IRAS 05189−2524) has a low derived age, and this is opposite from the effect expected if there is a simple evolutionary path from cool to warm ULIRG. Likewise, there is no trend of gas mass fraction with M/L_K. The most likely explanation is that our model where one starburst characterises the entire evolution of a ULIRG is too simplistic. Models of merging galaxies in fact indicate several burst events, first when the galaxies have their first encounter (as represented by IRAS 17208−0014) and then when they have their final merging event (as exemplified by IRAS 05189−2524). While M/L_K would still be time-dependent in this model, the derived age is only the age since the most recent starburst event. Since our data shows that the circumnuclear starburst in IRAS 05189−2524 is quite young, this explanation suggests that its final merging event occurred only recently.

4.5 Conclusions and outlook

We have analysed the stellar kinematics of 6 ULIRGs using high resolution near-IR integral field spectroscopy. Our main findings are as follows:

1. The ULIRGs in this study have low central K-band mass-to-light ratios, $< 0.3\,M_\odot/L_{K,\odot}$, and even $< 0.1\,M_\odot/L_{K,\odot}$ for several objects. These values are significantly lower than those of evolved elliptical galaxies. Starburst ages related to these M/L_K-values range from ∼10-200 Myr.

2. We do not see evidence for an evolutionary connection between infrared colour (f_{25}/f_{60}) and the stellar K-band mass-to-light ratios (or derived starburst ages), and conclude that the M/L_K traces only the stage of the most recent starburst in the system, which is not easily related to the evolutionary stage of the total ULIRG system.

The ability of these data to trace the age of the most recent significant starburst event in ULIRGs opens the way to interesting new applications in the modelling of these systems. Star formation in ULIRGs occurs in very dense regions and as a result, a large fraction of the star formation occurs in compact or ultracompact HII regions. In this situation, a large fraction of the Lyman continuum photons are absorbed by dust in the HII regions and not used for photoionization. As a result, models for ULIRGs based on standard photoionization methods (e.g., Starburst99) will fail. Since M/L_K as derived here does not depend on photoionization, it will circumvent this problem and readily provide an age determination for the most recent starburst. This application will be explored in a future paper.

References

Bender, R., Burstein, D., & Faber, S. M. 1992, ApJ, 399, 462

Bonnet, H., Abuter, R., Baker, A., et al. 2004, The Messenger, 117, 17

Cappellari, M. & Emsellem, E. 2004, PASP, 116, 138

Chung, A., Narayanan, G., Yun, M. S., Heyer, M., & Erickson, N. R. 2009, AJ, 138, 858

Dasyra, K. M., Tacconi, L. J., Davies, R. I., et al. 2006, ApJ, 651, 835

Davies, R. I., Sánchez, F. M., Genzel, R., et al. 2007, ApJ, 671, 1388

Downes, D. & Solomon, P. M. 1998, ApJ, 507, 615

Eisenhauer, F., Abuter, R., Bickert, K., et al. 2003, in Proceedings of the SPIE, Vol. 4841, Instrument Design and Performance for Optical/Infrared Ground-based Telescopes., ed. M. Iye & A. F. M. Moorwood, 1548–1561

Engel, H., Davies, R. I., Genzel, R., et al. 2011, ApJ, 729, 58

Farrah, D., Afonso, J., Efstathiou, A., et al. 2003, MNRAS, 343, 585

Ferrarese, L. & Merritt, D. 2000, ApJ, 539, L9

Gebhardt, K., Bender, R., Bower, G., et al. 2000, ApJ, 539, L13

Genzel, R., Tacconi, L. J., Rigopoulou, D., Lutz, D., & Tecza, M. 2001, ApJ, 563, 527
Hernquist, L. 1990, ApJ, 356, 359
Hummer, D. G. & Storey, P. J. 1987, MNRAS, 224, 801
Leitherer, C., Schaerer, D., Goldader, J. D., et al. 1999, ApJS, 123, 3
Magorrian, J., Tremaine, S., Richstone, D., et al. 1998, AJ, 115, 2285
Nardini, E., Risaliti, G., Salvati, M., et al. 2009, MNRAS, 399, 1373
Sanders, D. B., Mazzarella, J. M., Kim, D.-C., Surace, J. A., & Soifer, B. T. 2003, AJ, 126, 1607
Sanders, D. B., Soifer, B. T., Elias, J. H., et al. 1988, ApJ, 325, 74
Severgnini, P., Risaliti, G., Marconi, A., Maiolino, R., & Salvati, M. 2001, A&A, 368, 44
Tacconi, L. J., Genzel, R., Lutz, D., et al. 2002, ApJ, 580, 73
Temi, P., Brighenti, F., & Mathews, W. G. 2008, ApJ, 672, 244
Vázquez, G. A. & Leitherer, C. 2005, ApJ, 621, 695